

## Extracting Multiyear Surface Currents from Sequential Thermal Imagery Using the Maximum Cross-Correlation Technique

MELISSA M. BOWEN

*Colorado Center for Astrodynamics Research, University of Colorado, Boulder, Colorado, and National Institute of Water and Atmospheric Research, Auckland, New Zealand*

WILLIAM J. EMERY

*Colorado Center for Astrodynamics Research, University of Colorado, Boulder, Colorado*

JOHN L. WILKIN\*

*National Institute of Water and Atmospheric Research, Auckland, New Zealand*

PAUL C. TILDESLEY AND IAN J. BARTON

*CSIRO Marine Research, Hobart, Tasmania, Australia*

REBECCA KNEWTSON

*Colorado Center for Astrodynamics Research, University of Colorado, and Ball Aerospace and Technologies Corp., Boulder, Colorado*

(Manuscript received 7 August 2001, in final form 13 March 2002)

### ABSTRACT

Ocean surface circulation can be estimated by automated tracking of thermal infrared features in pairs of sequential satellite imagery. A 7-yr time series of velocity, extracted from thermal imagery of the East Australian Current using the maximum cross-correlation (MCC) technique, provides enough measurements for a more statistical evaluation of the method than has previously been possible. Excluding 1 yr with extensive cloud cover, the method produces about 8000 velocity estimates per month with some seasonal variation. Method precision is estimated to be between 0.08 and 0.2 m s<sup>-1</sup> rms, the lower value with more restrictive compositing. Mean flow, time-dependent flow, and eddy kinetic energy from the time series are compared with values derived from a dynamic height climatology, altimeter analyses, and drifter datasets in the region. The observations reproduce similar features in the flow. The differences between the observations are discussed in relation to noise in the methods and differences in the types of velocities they measure.

### 1. Introduction

Over the last three decades oceanographers have benefited from the frequent global coverage of infrared brightness temperatures (BTs) of the sea surface measured by satellite-borne radiometers. In addition to the routine derivation of sea surface temperature (SST), infrared satellite data have been used to estimate the surface circulation by calculating the motion of the thermal features in successive images (Emery et al. 1986; Holyer

and Peckinpaugh 1989; Kelly 1989; Cote and Tatnall 1995). There are compelling reasons to develop this technique into a robust, routine analysis: the spatial and temporal coverage of velocities derived from thermal imagery would complement both conventional shipboard and moored observations and those derived from satellite altimeter measurements.

Velocity was first estimated in a sequence of images by tracking features by eye, a method which is subjective, as the results may not be repeated by another person, and impractical for the routine analysis of large datasets. Greater computer power has allowed many automated feature-tracking methods to develop that use a suite of criteria, such as wavelets (Liu 1997), gradient thresholds (Holyer and Peckinpaugh 1989), and neural networks (Cote and Tatnall 1995) to identify features in sequential images. These methods require consider-

---

\* Current affiliation: Institute of Marine and Coastal Sciences, Rutgers University, New Brunswick, New Jersey.

---

Corresponding author address: Dr. Melissa M. Bowen, NIWA, P.O. Box 14-901, Kilbirnie, Wellington, New Zealand.  
E-mail: m.bowen@niwa.cri.nz.

able user input to determine criteria that define certain features and, in some cases, extensive preparation of imagery. The maximum cross-correlation (MCC) technique (Schmetz and Nuret 1987; Emery et al. 1986; Kelly and Strub 1992) is a more straightforward method of pattern tracking that requires less user input. The method matches patterns in all possible subwindows of one image with those in a sequential image, avoiding the computational problems of searching for specific features. Areas of weak pattern tracking can be rejected automatically in postprocessing of the velocities, reducing the level of human involvement other feature-tracking methods require.

Velocities from the MCC method have also been compared to velocities derived in a different manner from sequential thermal imagery. A number of authors find velocities by inverting a heat equation to find the displacements most likely to produce the changes in temperature between two images (Kelly 1989; Zavialov et al. 1998; Vigan et al. 2000a,b). Kelly and Strub (1992) found that the inversion method produced virtually the same velocities as the MCC technique for considerably more effort. The simplicity of the MCC method, compared to other feature-tracking techniques and the inversion method, recommend it for the routine extraction of long velocity time series from thermal imagery.

Although the basic technique is straightforward, interpreting the results is not as clear. Only a small number of sequential images have been used in tests of the MCC method (or any other feature-tracking method) and few ancillary measurements exist to compare to the velocities. Tokmakian et al. (1990) evaluated the method by comparing MCC velocities from a short image sequence with dynamic height and ADCP measurements and by comparing MCC velocities derived from a short sequence of synthetic images with model fields. They suggest noise in the feature-tracking method is between 0.1 and 0.25 m s<sup>-1</sup> rms. Kelly and Strub (1992), also using imagery from the California Current region, found MCC velocity magnitudes were 35% lower than ADCP velocities and about 55% lower than drifter velocities over 2.5 days. They noted that the comparison of all three velocity measurements illustrated only how widely sampling techniques could differ and still be useful. Although they make a good point, the oceanographer is left uncertain as to how much can be gained by extracting MCC velocities from thermal imagery.

Here we apply the technique to 7 yr of thermal imagery from the East Australian Current (EAC) region and derive several empirical measures of the method. The high density of current measurements, made possible by an archive of almost every satellite pass over the area, allows us to estimate noise in the method as well as compare the velocities with other multiyear datasets in the region. We begin with a discussion of the MCC method, show velocities derived from the East Australian thermal imagery, and estimate method precision. Finally, we compare the MCC velocities with

velocities from climatology, drifters, and altimeter measurements in the region and summarize our results.

## 2. Methods

### a. Observations

Satellite infrared images were obtained from the Advanced Very High Resolution Radiometer (AVHRR) flying on the National Oceanic and Atmospheric Administration polar-orbiting satellites. The High Resolution Picture Transmission data were downloaded from the satellites as they flew over a receiving station at the Commonwealth Scientific and Industrial Research Organisation (CSIRO) located at Hobart, Australia. The higher-resolution images (about 1 km) available directly from the satellite are preferable to the more widely available lower-resolution (about 4 km) Global Area Coverage data, primarily because they allow the displacement of features to be determined to greater accuracy.

The passes were geolocated with a package developed at CSIRO. The navigation software solves for an orbital trajectory that minimizes the offsets of observable coastline from a template coastline over a period of about 10 days. The attitude model assumes no error in pitch and constant yaw and roll error in each pass over the receiving station. The accuracy of the navigation is estimated at about 1 km rms, based on residuals from the coastline fit.

Any errors in geolocation between a pair of images will appear as a spurious velocity when determining the displacement of thermal features. A 1-km rms error in the displacement between images separated by 8 h, an average time separation, will result in a 0.05 m s<sup>-1</sup> rms error. Errors of this magnitude are small compared to most of the currents we expect in the EAC.

Clouds in the imagery must also be flagged to reduce spurious feature tracking. Clouds were detected in the imagery using a method based on Kriebel et al. (1991), which utilizes a series of threshold tests on individual AVHRR channels as well as differences between the three infrared channels.

### b. The maximum cross-correlation technique

The movement of features between two images is estimated by computing the cross correlation of the temperature between windowed portions of the images. The first image is divided into subwindows (one such subwindow is shown schematically by the solid black box in Fig. 1) and the cross correlation computed between each subwindow in the first image and subwindow-sized portions of the second image. Cross correlations are computed in a search area (dashed box) corresponding to the largest expected displacement of the features from their location in the first image. The location of the subwindow in the second image that produces the highest cross correlation with the subwindow in the first

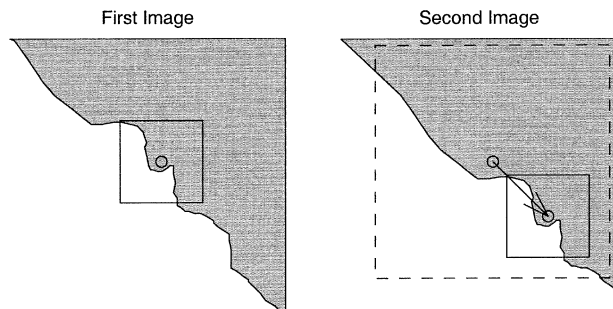


FIG. 1. Schematic of two successive images showing the location of a subwindow in the first image (solid box) and the location of the best match in the second image (solid box). The best match is found by computing the cross correlation between the subwindow from the first image and each subwindow-sized section within the search area in the second image (dashed box) and choosing the position with highest cross-correlation value. The velocity is the displacement divided by the time between the images.

image (solid box in second image) indicates the most likely displacement of the thermal features (arrow). The velocity is the displacement divided by the time separation between the images.

The method has two main parameters: the size of the subwindow and the extent of the search in the second image. The size of the subwindow is a balance between containing enough features for tracking and smoothing out the structure of the flow. Spatially filtering the images and repeating the feature tracking showed that features between 10 and 20 km scale provide much of the tracking. These scales are most likely produced by wind, solar radiation, and instabilities that break geostrophic constraints but are being carried by the larger-scale flows. We attempted to find a justification for subwindow size, as well as other method parameters, using output from a 1-km resolution, three-dimensional ocean model, but were unable to create the necessary temperature scales or maintain them when they were introduced. Lacking a model test for the subwindow size, we chose to use a square with 30-km sides, which appeared to visually strike the balance better than 20 or 40-km square subwindows. We note that the MCC technique has been used successfully in many different ocean regions with a range of subwindow sizes, generally between 25 and 50 km, most often in the 30–40-km range (Domingues et al. 2000; Emery et al. 1992; Tokmakian et al. 1990; Kelly and Strub 1992).

The search area, or range, over which to search in the second image is determined by the speed of the expected currents. In the EAC region the range is determined for each image pair, based on the time separation between the images, to capture currents of at least  $1 \text{ m s}^{-1}$ . Velocities were derived from all image pairs having time separations between 3 and 13 h. Both Tokmakian et al. (1990) and Emery et al. (1992) find the MCC velocities are most successfully derived when the time between images is 12 h or less.

Cross correlations are calculated if 60% of the pixels

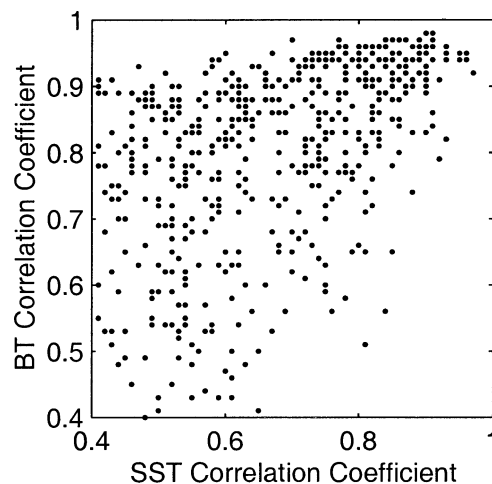


FIG. 2. Maximum correlation coefficients of SST plotted vs BT show that the BT coefficients tend to be higher, which indicates better pattern tracking.

in a subwindow are within a range corresponding to the surface thermal signal (we specify  $8^{\circ}$ – $25^{\circ}\text{C}$  for the EAC region). This tolerance allows thermal patterns in areas with some cloud cover to still be successfully tracked. In addition, denser velocity coverage was produced, at the expense of statistical independence, by overlapping subwindows by 15 km.

### c. Feature tracking with brightness temperatures (BTs) versus SST

We found that imagery from the AVHRR channel 4 ( $10.8 \mu\text{m}$ ) produced more robust feature tracking than imagery derived from a multichannel SST product. Velocities computed using several pairs of concurrent channel 4 BT and SST images from the east coast of Australia and the coast of California were often in different directions. The individual correlation coefficient distributions were similar in shape, but had maxima slightly displaced relative to one another. The maximum correlation coefficients from velocities computed with BT were consistently higher than those from SST (Fig. 2), indicating more robust pattern tracking in the BT images.

The feature tracking is likely more robust in BT images because they contain less noise than SST images. The lower the noise in two signals, the closer the correlation coefficient to the noise-free value (Emery and Thomson 1998). Additional noise can arise in SST because it is derived using the difference of temperatures from AVHRR channels 4 and 5. Differencing increases the noise in the SST if noise in the individual channels is uncorrelated and decreases it if the noise is correlated.

To gauge the effect of noise in channels 4 and 5 on the SST, the error variance was derived from a multichannel SST algorithm and values calculated for a range of zenith angles and temperatures. Assuming the noise

in channels 4 and 5 is equal and uncorrelated, the noise in SST is about 3 times greater than the individual channels. If the noise is correlated, error in SST is reduced by only 5% from the individual channels. Therefore, even a small amount of uncorrelated noise in the individual channels will be amplified in the SST images and lead to smaller correlation coefficients when feature tracking.

Since the MCC method relies only on variations of temperature within a subwindow, not the accuracy of the SST, images derived from channel 4 are preferable over the multichannel SST or channel 5 alone (which has less infrared signal from sea surface temperatures than channel 4). Similarly, when deriving thermal gradients Strub et al. (1997) also advocate using channel 4 BT to avoid introducing additional noise. All of our analysis was done using channel 4 BT imagery.

#### d. Filtering the vectors

After all possible vectors have been derived from an image pair, several filters are applied to improve the quality of the velocities. We use two filters, first removing velocities resulting from poor pattern matches and then requiring a degree of spatial coherence in the velocity field.

Velocities produced by weak feature tracking can be removed by keeping vectors associated with only the highest maximum correlation coefficients. We determined a level for rejecting coincidental pattern matches by correlating images from four different ocean regions with one another and finding the 95 percentile of the maximum correlation coefficients. Since all the correlations are random pattern matches, the 95 percentile can be used as a cutoff when correlating sequential images to ensure that most of random pattern matches are rejected. The cutoff value starts at 0.6 for a range of 5 km and increases with increasing range (Fig. 3) as the chance for higher spurious maximum cross-correlation coefficients increases. Our values are consistent with those recommended by Kelly and Strub (1992) who performed a similar analysis using imagery from the California coast.

Second, vectors are also filtered by requiring some spatial coherence. Each velocity is required to agree within a specified amount with a specified number of the neighboring vectors or it is removed. In this study, we required each vector have two immediate neighbors with displacements matching within 5 km. These numbers were chosen by testing the filter on a subset of data and picking the values that appeared to best remove randomly oriented vectors embedded in the more coherent ocean circulation patterns. This is a somewhat subjective choice and other users of the technique should regard these parameters as a starting point, experimenting and altering as they see fit [e.g., see Barton (2002) for another filtering technique].

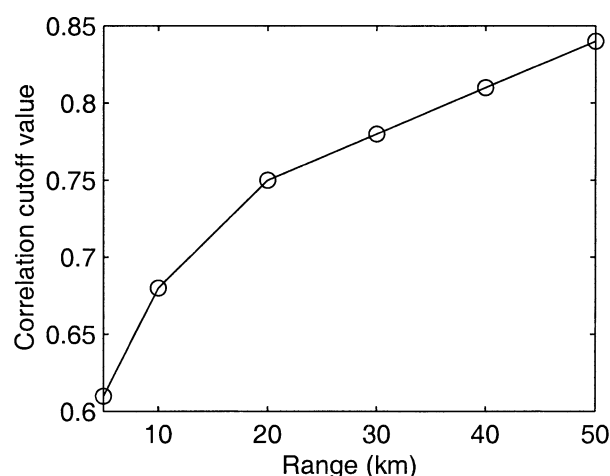


FIG. 3. Value of the correlation cutoff as a function of the search range. Higher-correlation cutoffs reflect greater chances of obtaining a high-correlation coefficient by chance.

### 3. Results

#### a. Data distribution

Feature tracking in pairs of sequential images produces velocities in regions where both images are cloud free and thermal features are prominent enough to track. Velocities from a particularly clear image pair show the level of detail that can be resolved by the method (Fig. 4). Two warm tongues of water extend southward and have almost entirely enclosed a triangular region of colder water. Strong anticyclonic circulations around the warmer tongues and cyclonic circulation around the colder enclosed water correspond to the directions expected from a geostrophic balance. Feature tracking is most successful along the edges of the warm tongues, where thermal gradients are strongest, and poor in the centers of the tongues, where thermal gradients are weakest.

The number of velocities that can be extracted from the thermal imagery also varies widely in time. Some seasonal signal is evident in the number of velocity vectors per month over the entire time series (Fig. 5), probably the result of seasonal cloud cover. August through January have considerably more cloud-free periods and produce more vectors than other months. Most striking is the large reduction in vectors in 1999 due to the cloud cover associated with a strong La Niña. Due to the poor return in 1999, further analyses with the MCC velocities exclude this year. Excluding 1999, an average of 8000 vectors per month can be expected over the roughly  $1.5 \times 10^6 \text{ km}^2$  of ocean.

Examining the velocities by spatial distribution shows measurements are more concentrated near the Australian coast, dropping off with distance away from the coast (Fig. 6). The larger number of measurements are partially due to the frequent occurrence of a cloud-free strip extending along the coast, presumably caused by dry



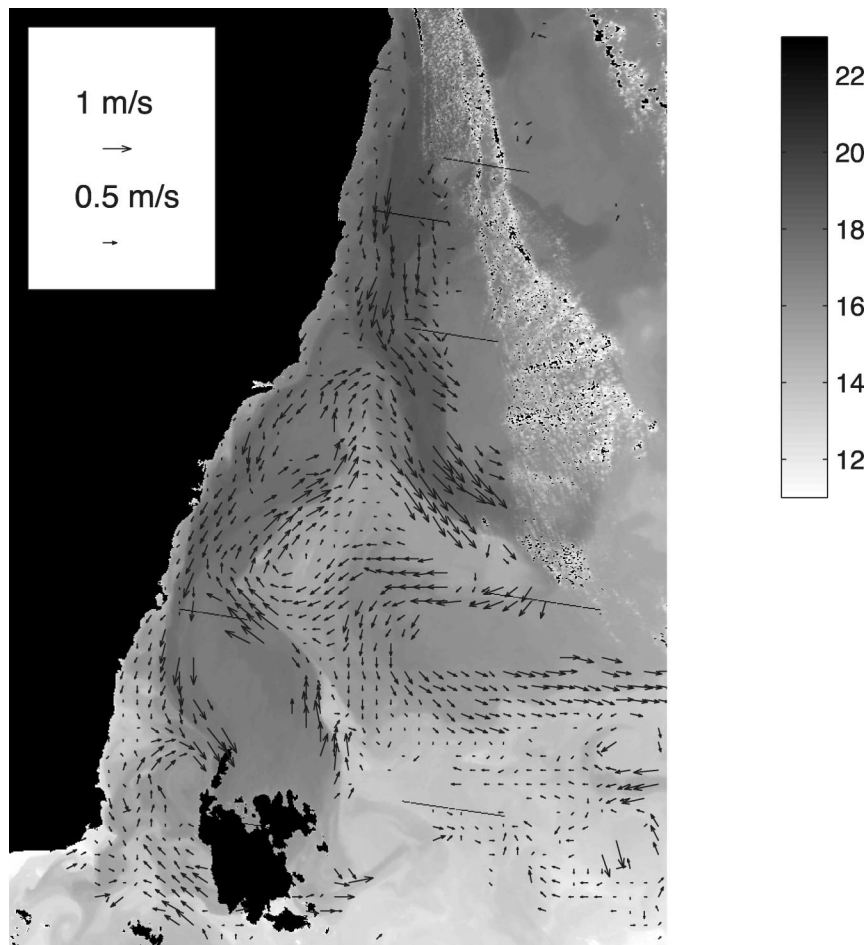


FIG. 4. MCC velocities, derived from a pair of thermal images on 16 Aug 1997, show the formation of a cyclonic eddy as a warm arm of the East Australian Current wraps around a triangular region of cooler water. Clouds and land show up as black regions in the thermal image plotted underneath, as do a few lines of data dropouts.

winds from the land. The strongest thermal gradients are also found near the coast and in the region where the current separates from the coast (roughly  $32^{\circ}$ – $36^{\circ}$ S), which contributes to the dense sampling.

#### *b. Velocity composites*

Patchiness in the velocities due to intermittent cloud cover can be reduced by making a composite over sev-

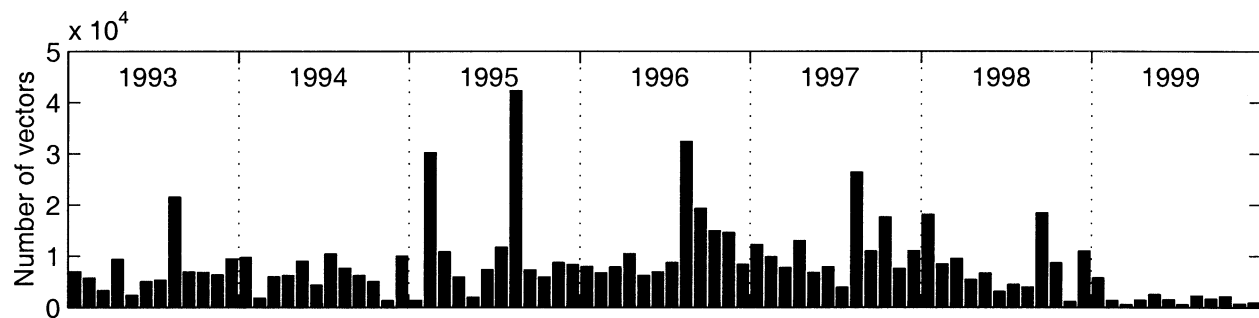


FIG. 5. Number of MCC velocity vectors extracted from the EAC region binned by month. In general, the spring and summer months produce more vectors. Observations of the sea surface were considerably reduced throughout 1999 due to greater cloud cover.

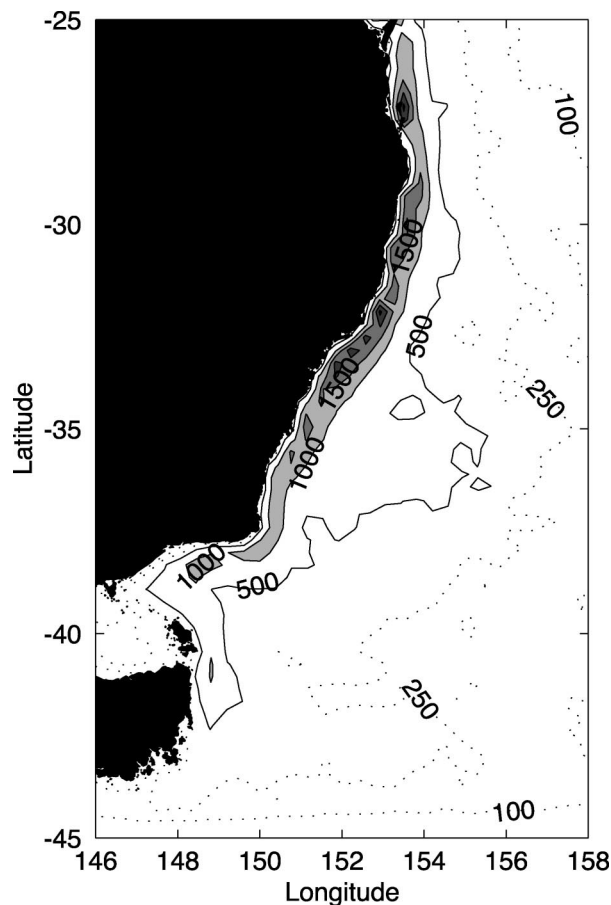


FIG. 6. Number of vectors binned by location for 1993–99. Sampling is more frequent at the coast where thermal gradients are strongest and cloud cover less prevalent.

eral days. The clouds tend to move quickly over a day or two while the underlying ocean circulation remains relatively constant. The second panel of Fig. 7 shows a 3-day composite in 30-km bins centered on 16 August 1997, which contains the vectors in Fig. 4. Velocities from image pairs over the entire 3 days have filled in blank areas in Fig. 4 where weak thermal gradients and clouds prevent feature tracking.

A time series of composites show the evolution of the mesoscale features given several relatively cloud-free weeks. In the first composite a warm tongue extends down the coast and another branches directly offshore farther north. Velocities in the colder water seaward of the warm tongue are directed westward, starting the formation of the cyclonic eddy seen clearly in the second composite. Velocities at the bottom edge of the cooler triangular region are mostly westward, bridging the gap between the two warmer tongues. In the next two composites the cooler water moves farther west and the southernmost portion of the warm tongue is pinched off. As the cooler water progresses toward the coast the strong southward velocities at the coast slow down and change to northward flow.

In addition to producing more complete pictures of the circulation, making composites also condenses the large number of velocities into a dataset that is easier to handle. The velocities can also be placed on a specific grid in space and time for comparison or combination with other measurements.

Velocities were averaged over a variety of day lengths with a specified minimum number of velocities in each composite velocity. The results are particularly sensitive to the choice of the minimum number of velocities in a composite. Raising the minimum reduces the number of vectors; however, they are more representative of an average over the time period and contain less noise. We will show results from two types of 3-day composites: a lower threshold case, where all composite velocities are kept regardless of number of velocities that went into them, and a higher threshold case, where three velocities are required in a 30-km box over the 3-day period before the composite velocity is kept.

### c. Estimates of method noise from covariance functions

The precision of the MCC method is estimated by computing lagged covariances of the velocities in space or time, binning them according to lag, and averaging over all the values. If the noise in the velocities is uncorrelated, it should average out in the covariance at all lags except at zero lag. In other words, the covariance should reflect the signal variance at all lags except at zero lag where the variance is a sum of the noise and the signal variances. The noise in the method can be estimated from the jump between the computed covariance at zero lag and the extrapolated value of the signal variance at zero lag.

The raw vectors were subsampled to a 30 km  $\times$  30 km grid to ensure that each velocity was independent and composites calculated in 3-day segments. Covariances were derived from each composite by lagging velocity measurements in space, multiplying them, and binning the results by the lag in distance. The process was repeated for each composite and the covariances within a bin averaged (Fig. 8).

To estimate the value of the signal variance at the origin, a velocity covariance of the functional form proposed by LeTraon and Hernandez (1992) has been fit to the lagged covariances of both components of velocity. The difference between the estimated zero crossing from the LeTraon and Hernandez (1992) function and the observed value suggests that velocities derived in this manner are precise to about 0.2 m s<sup>-1</sup> rms. Other ways of estimating the zero crossing with other functional forms produced only small differences.

An estimate of the noise variance was made in a similar manner with the velocities from the higher threshold composites. The variance at all lags is reduced (Fig. 9). The estimated signal variance is reduced by about 20%. Apparent method precision, from fitting the

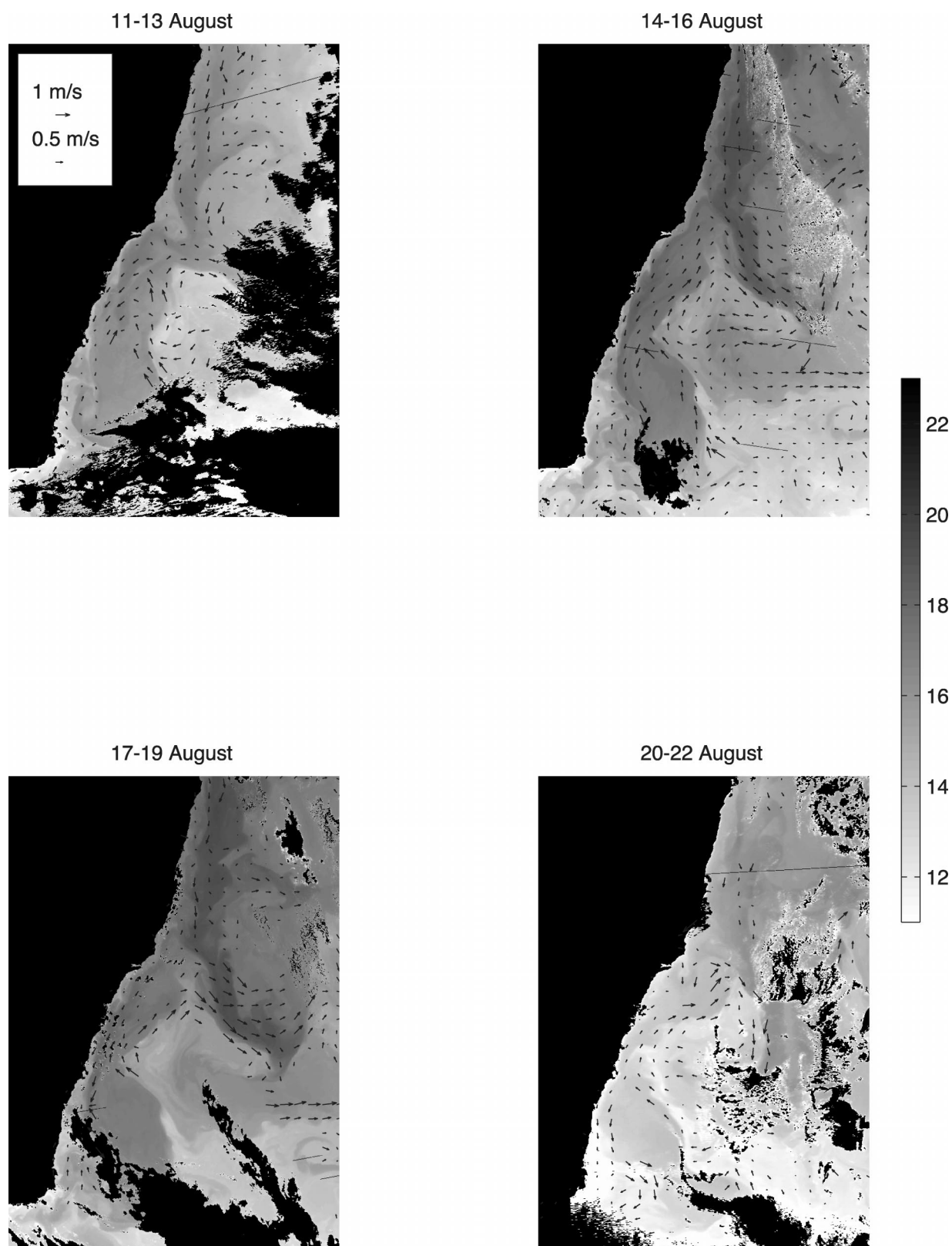


FIG. 7. A series of 3-day composites of MCC velocities from August 1997, each plotted on top of a thermal image within the time period, show the evolution of a strong cyclone as a seaward warm tongue moves westward, trapping a triangular region of cooler water, and pinching off a warm tongue of water against the coast.

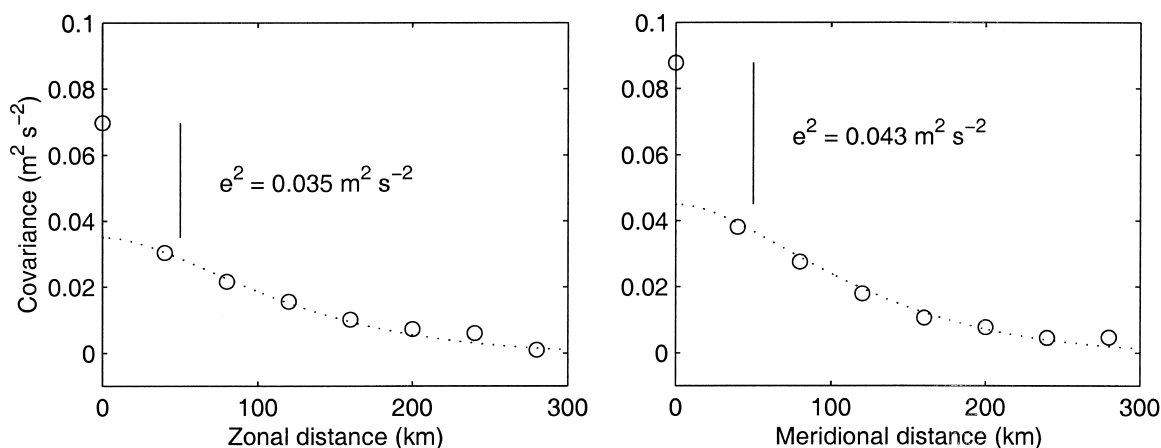


FIG. 8. Lagged covariance of the (left) zonal velocity in the zonal direction and (right) meridional velocity in the meridional direction from the lower threshold composites.

same functional form, is about  $0.08 \text{ m s}^{-1}$  rms, a factor of 2 less than the previous estimates. Presumably requiring more vectors in the composite velocities has reduced the noise in the measurements and removed some signal associated with variability at timescales less than 3 days.

#### 4. Comparison of the MCC currents with other observations

##### a. Mean flow

The MCC currents were averaged over the 6-yr time series and compared to currents calculated from the dynamic height relative to 2000-m depth from the CSIRO Atlas of Regional Seas (CARS) climatology (Fig. 10) (Ridgway et al. 2002). The mean MCC velocities are similar whether they are calculated from the velocities before composites are made or from the different types of composites. An arbitrary choice was made to show only velocities where there are more than 40 degrees of

freedom in the sampling [where the degrees of freedom are the number of 10-day segments sampled based on a characteristic timescale in the region (Wilkin et al. 2002)].

The MCC and CARS mean flows share several features. The velocities are remarkably similar in the northern part of the region. Both show southward velocities of about  $0.4 \text{ m s}^{-1}$  close to the coast where a persistent current is reliably found (Nilsson and Cresswell 1981; Godfrey et al. 1980). Farther eastward, the southward flows in both datasets are about  $0.15 \text{ m s}^{-1}$ , drop to near zero, and then show weak reversal to northward flows about 100 km from the coast.

Farther south, in the region where the main current separates from the coast (Godfrey et al. 1980), both observations show a bifurcation of the southward flow. One arm of the flow continues south along the coast and the other turns eastward. The greatest difference between the two datasets is in the magnitude of the eastward arm of the flow near  $34.5^\circ\text{S}$ ,  $155^\circ\text{E}$ . The CARS

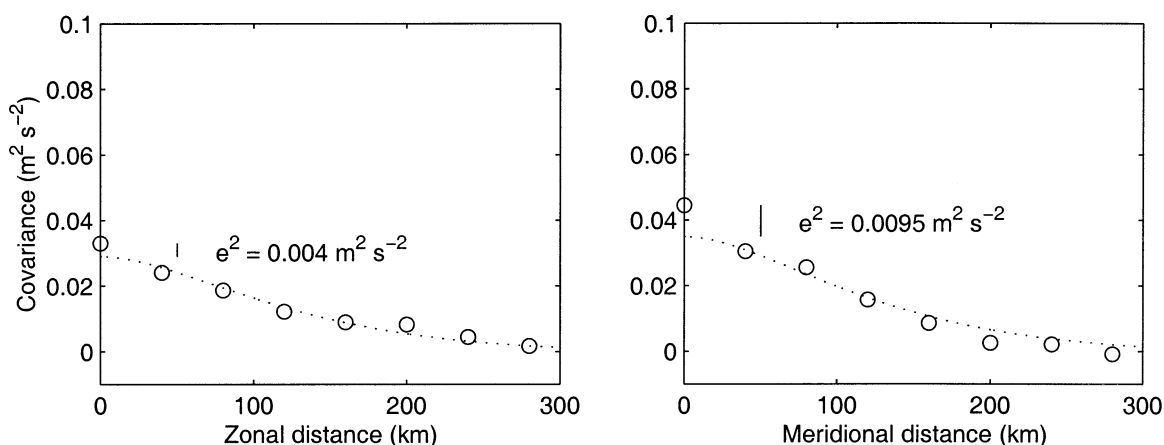


FIG. 9. Lagged covariance of the (left) zonal velocity in the zonal direction and (right) meridional velocity in the meridional direction using covariances from composites with the higher threshold.



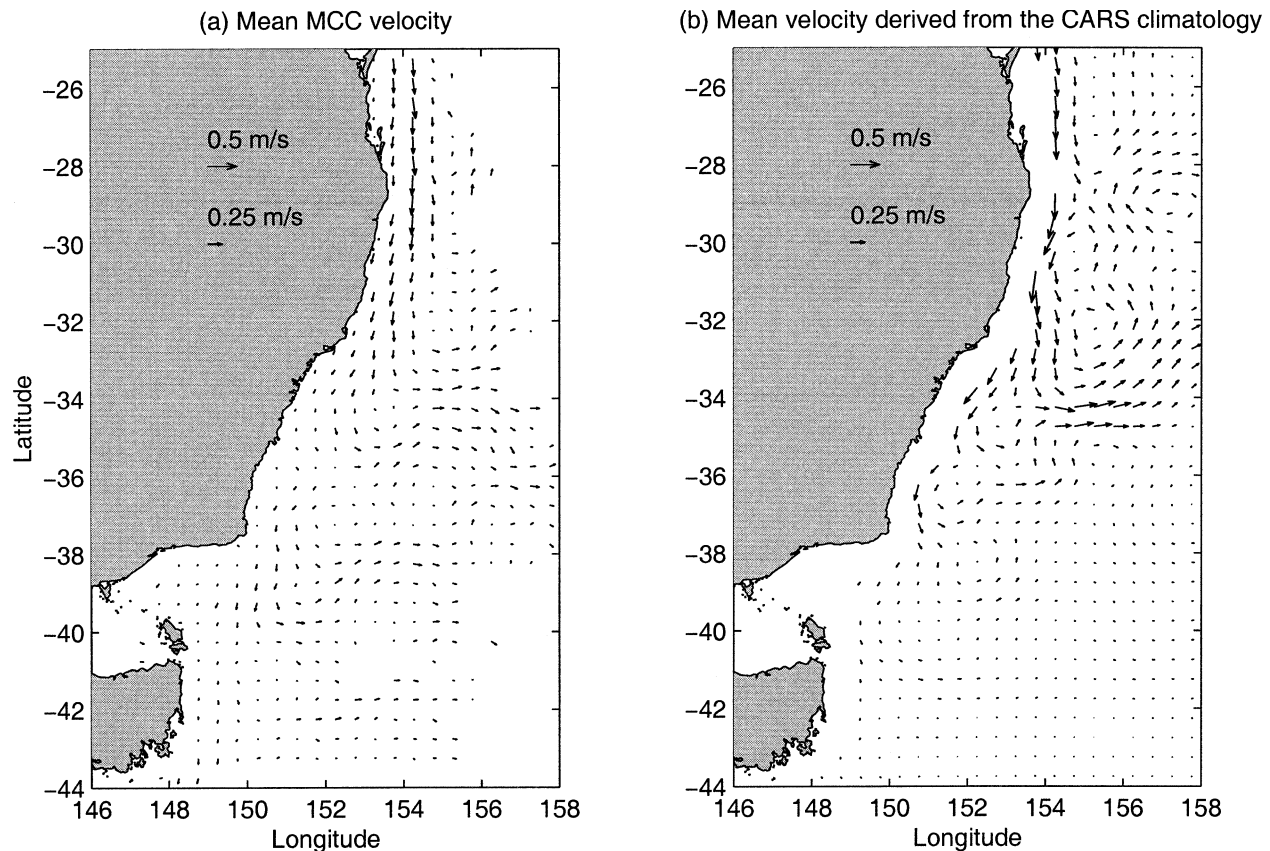


FIG. 10. The 6-yr mean velocity (1993–98) from (a) the MCC velocities and (b) the velocity calculated from dynamic height relative to 2000 m from the CARS climatology. Both show strong southward flows along the coast turning eastward between  $32^{\circ}$  and  $34^{\circ}$ S. Southward and eastward flows of weaker magnitudes are found farther to the south.

climatology shows an offshore jet of strength equal to the mean coastal current farther north. The average MCC velocity is weaker. There are a number of reasons a difference between the velocities might occur. Although most of the EAC region is heavily sampled in the CARS climatology (Ridgway et al. 2002), this particular location is at the edge of the heavy sampling and the velocities might be affected by the nearby sparse data distribution. In addition, the velocities have been derived from the CARS dataset assuming the flow at 2000 m depth is negligible, an assumption that current meter records show may often be invalid (Mata et al. 2000).

South of the separation region the circulation is dominated by the mesoscale with intense cyclones and anticyclones forming (Nilsson and Cresswell 1981). Not surprisingly, the mean flow in both datasets is weak. Flow near the coast continues southward with regions of eastward circulation farther seaward. The locations of the eastward flows differ between the datasets, but both show weak flows of generally less than  $0.2 \text{ m s}^{-1}$ .

#### b. Time-dependent circulation

The only dataset in the region with spatial and temporal coverage similar to the MCC velocities

are time series of sea surface height from the TOPEX/Poseidon (T/P) altimeter. The 6-yr mean from the MCC velocities was subtracted and the anomaly velocities compared to geostrophic velocities computed from the altimeter sea surface height anomalies. Sea surface heights were filtered over approximately 65 km, or 11 along-track points, and geostrophic velocities computed from along-track differences at that scale. The choice of filter length was guided by the comparisons of altimeter-derived and in situ velocities in Strub et al. (1997). Any MCC velocity that fell within 1 day and 20 km of an altimetric velocity was projected into the altimeter across-track direction and the velocity components compared.

Over the 6 yr of data, more than 2000 comparisons were made between altimetric velocities and velocities from the MCC composites. The rms differences between the altimetric and MCC velocities were  $0.25 \text{ m s}^{-1}$  for the lower-threshold and  $0.3 \text{ m s}^{-1}$  for the higher-threshold composites. These numbers are higher than the estimates of noise in the MCC method ( $0.2$  and  $0.08 \text{ m s}^{-1}$  for the low and high composites, respectively) and the estimated accuracy of anomaly geostrophic velocities from the altimeter sea surface heights is  $0.07 \text{ m s}^{-1}$ ,

based on an error of 0.03 m in height anomaly, the along-track distance, gravity, and the Coriolis parameter.

Differences in the way the velocities are sampled should also contribute to the difference between the two sets of observations. First, the MCC velocities should be more representative of the average over a subwindow, while the altimeter velocities are derived from a narrower strip along the ground track. Presumably with smaller spatial sampling the altimeter-derived velocities would be biased faster relative to the MCC velocities. However, a regression of the MCC and altimetric velocity components, accounting for imprecision in both measurements methods, indicates no measurable scale bias between the two types of velocity observations. Second, the MCC velocities probably contain some ageostrophic flows that have survived the composite process, as well as geostrophic flows. Ekman velocities, for example, may persist over the composite period and contribute to a randomly oriented disagreement with the geostrophic velocities from the altimeter.

Correspondence between the altimetric and MCC velocity components was also gauged by calculating correlation coefficients. The correlation coefficient between the lower-threshold composites and the altimeter-derived velocities is 0.49. The higher-threshold composites are more highly correlated at 0.63. The values are in the range of correlation coefficients calculated by Ohlmann et al. (2001) between drifting buoy velocities and altimeter velocities in the Gulf of Mexico for a variety of water depths and filtering of the altimeter data. In particular, the correlation coefficients from the higher-threshold composites are in the range of the highest correlation coefficients found by Ohlmann et al. (2001).

### c. Eddy statistics

Variance ellipses were calculated from the 6 yr of MCC velocities by removing the mean velocity and finding the principal axes of the variances in 60-km bins (Fig. 11a). As seen in the covariance plots in Fig. 8, squaring the velocity preserves the noise as well as the signal variance. To correct for this effect, the noise estimated earlier was subtracted from the squared velocities. Ellipses with significant anisotropy are shaded. The lower-threshold composites are used. However, once the noise variances are removed, the eddy kinetic energies from the high- and low-threshold composites are nearly identical.

Eddy kinetic energy peaks about 300 km away from the coast with highest magnitudes slightly over  $0.1 \text{ m}^2 \text{ s}^{-2}$ . The most energetic region corresponds to where the current separates from the coast and the region of intense eddy formation slightly south of it (Nilsson and Cresswell 1981). Energies of at least half that value extend northward to  $25^\circ\text{S}$  and to the southeast corner of Australia. South of the Australian continent and east of Tasmania kinetic energy is nearly an order of magnitude less than in the separation region to the north.

Velocity fluctuations nearest the coast are aligned parallel with the coast, especially in the northern region where the current consistently follows the coastline. In the separation region near  $32^\circ\text{S}$ , fluctuations are directed more offshore. South of this region the variance ellipses reflect the pattern of the eddies propagating down the coastline. Closer to the coast fluctuations are alongshore, while farther out the velocities are directed offshore. At a distance of about 200 km (the eddy diameter scale) the ellipses turn to a more alongshore direction again.

Variance ellipses were also derived from geostrophic velocities calculated from the T/P altimeter sea surface heights (Fig. 11b) at locations where ascending and descending altimeter tracks cross one another. After deriving velocities from sea surface heights in the manner previously described, velocities from each track were linearly interpolated to a common time base, and the full velocity vectors determined from the two across-track velocity components. A velocity variance of  $0.01 \text{ m}^2 \text{ s}^{-2}$  was subtracted to account for uncertainty in deriving full velocity from the two components. Uncertainties in the full velocity due to temporal interpolation were not estimated. Ellipses with values smaller than the noise estimate are not plotted.

Eddy kinetic energies derived from the altimeter measurements are also higher in the vicinity of the separation region and directly south of it. The magnitudes of the highest energies are not significantly different from the highest magnitudes derived from the MCC velocities. The altimeter-derived energies decrease slightly more rapidly away from the energetic region than the MCC velocities indicate. In particular, no significant energy is measurable at crossover points in the southwestern corner of the region. Variance ellipses at the crossover points closest to the coast are aligned predominantly in the along-shelf direction (Fig. 11b), but farther east of where the MCC ellipses are aligned parallel to the coast.

Variance ellipses were also derived from drifting buoy velocities from the World Ocean Circulation Experiment Surface Velocity Programme (Fig. 11c). Drifter velocities were binned in  $2^\circ \times 2^\circ$  squares and eddy kinetic energy calculated in bins with 10 or more degrees of freedom. Unfortunately for our purposes, the drifter distribution is biased toward regions of slower flows both because of the deployment locations of the drifters and because they remain longer in regions of slower flow. No noise estimates were subtracted from the kinetic energies because none could be reliably estimated.

Although resolution is limited, the drifters do show the same type of distribution seen in the MCC and altimeter-derived energies. Higher energies are found in the region where the current turns from the coast, with perhaps higher energies extending to the edge of the domain than the other measurements suggest. Given the degrees of freedom in the drifter dataset, few of the differences between these values and those of the altim-

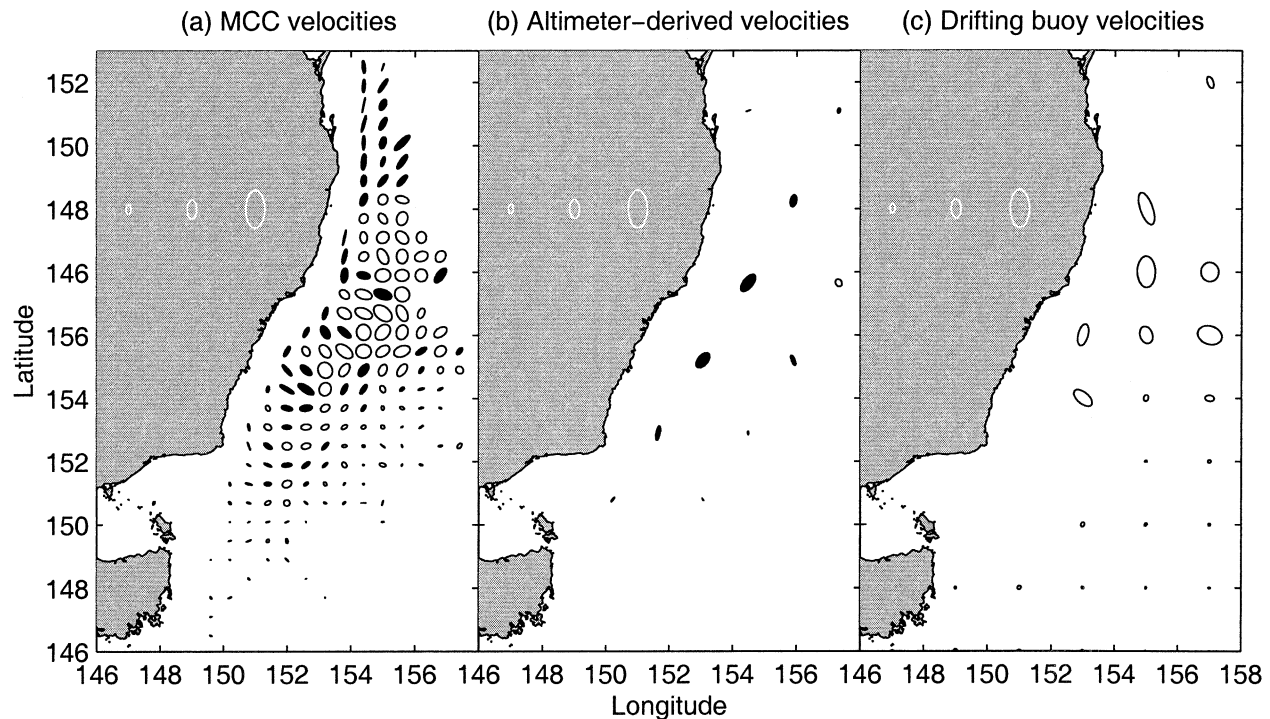


FIG. 11. Variance ellipses calculated from (a) the MCC velocities from the low threshold composites, (b) geostrophic velocity estimates at the crossover points of the TOPEX/Poseidon altimeter, and (c) drifting buoy data binned in  $2^\circ$  bins. Shading indicates ellipses with significant anisotropy. Scale ellipses have major axes corresponding to 0.05, 0.1, and  $0.2 \text{ m}^2 \text{ s}^{-2}$  with minor axes half those values.

eter and MCC velocities are significant, nor can significant anisotropy in the ellipses be discerned.

## 5. Summary discussion

The 7-yr time series of velocities we have extracted from thermal imagery is orders of magnitude longer than others previously derived using the MCC technique. The volume of observations allows a statistical evaluation of the method performance. On average, 8000 vectors per month are obtained in the East Australian region between 1993 and 1998, despite a climatological cloud cover of about 70%. Higher numbers of velocities were extracted in regions of lower cloud cover and persistent thermal gradients with some seasonal and interannual variation.

The precision of the method, estimated from lagged covariances of the composite velocities, is about  $0.2 \text{ m s}^{-1}$  rms decreasing to about  $0.08 \text{ m s}^{-1}$  rms with more restrictive compositing, or about 0.28 and  $0.12 \text{ m s}^{-1}$  rms in the magnitudes of the velocity. Our empirical estimates of method precision are slightly higher than the range of  $0.10\text{--}0.25 \text{ m s}^{-1}$  rms noise that Tokmakian et al. (1990) find in MCC velocity magnitudes by the advection of an AVHRR thermal image with surface velocities from an ocean model. An increase in noise is not surprising since temperature features are in reality evolving as well as being carried by a current. The empirical estimates do suggest, however, for only slightly

more restrictive compositing the noise in the method can be halved.

A comparison of the MCC velocities to other velocity estimates in the region gives a sense of how the advection of thermal features corresponds to other approximations of surface currents. The 6-yr mean MCC velocities show the same flow direction as the mean derived from a dynamic height climatology. Velocity magnitudes correspond most closely in the northern part of the domain where sampling in both distributions is denser and the current less variable.

The rms differences between time-dependent MCC velocities and geostrophic velocities derived from altimeter sea surface heights are greater than the estimates of precision in each method. There appears to be no scale bias between the two types of observations, in contrast to the bias of 30%–50% that Kelly and Strub (1992) report from their comparison of MCC velocities with those measured by drifter and ADCP. We suggest some of the differences in our comparison may arise from ageostrophic velocities in the MCC measurements. Consistent with this explanation, the correlation coefficients between the velocities lie in the range of those derived by Ohlmann et al. (2001) in comparisons between drifting buoy velocities and velocities derived from altimetry in the Gulf of Mexico.

Variance ellipses derived from the MCC, altimetric, and drifting buoy velocities all show higher kinetic energy of similar magnitudes in the separation region, al-



though the some of the orientations of the variance ellipses differ. The comparisons do illustrate the advantages of the spatial and temporal sampling of the MCC velocities. The MCC velocities are often more dense than the altimeter measurements and more widespread than drifting buoy deployments. The relative ease with which velocities can be extracted from thermal imagery, in comparison with other observational techniques, suggests that this method can be used to augment other observations in regions where it is feasible to do so.

In addition to use in real-time analyses, the technique can be applied to existing archives of infrared satellite data to estimate currents almost a decade before altimetric measurements. The number of regions where the method can be applied should also expand once global coverage of high-resolution thermal data is routinely available.

**Acknowledgments.** MB, WE, and RK were supported by a NASA *Jason-1* program grant. We would like to thank David Griffin at CSIRO, Hobart, for the use of a compiled drifter dataset and the CSIRO Division of Marine Research for providing AVHRR and altimeter data. Chuck Fowler and Dan Baldwin at the University of Colorado assisted with many aspects of the project. The MCC velocities were produced with the help of Chris Edsall and the supercomputer facility at the National Institute of Atmospheric and Water Research, Wellington, New Zealand. The authors would also like to thank two anonymous reviewers for their comments.

#### REFERENCES

- Barton, I. J., 2002: Ocean currents from successive satellite images: The reciprocal filtering technique. *J. Atmos. Oceanic Technol.*, **19**, 1677–1689.
- Cote, S., and A. R. L. Tatnall, 1995: The Hopfield neural network as a tool for feature tracking and recognition from satellite sensor images. *Int. J. Remote Sens.*, **18**, 871–885.
- Domingues, C. M., G. A. Goncalves, R. D. Ghisolfi, and C. A. E. Garcia, 2000: Advective surface velocities derived from sequential infrared images in the southwestern Atlantic Ocean. *J. Remote Sens.*, **73**, 218–226.
- Emery, W. J., and R. E. Thomson, 1998: *Data Analysis Methods in Physical Oceanography*. Pergamon, 634 pp.
- , A. C. Thomas, M. J. Collins, W. R. Crawford, and D. L. Mackas, 1986: An objective method for computing advective surface velocities from sequential infrared satellite images. *J. Geophys. Res.*, **91**, 12 865–12 878.
- , C. Fowler, and C. A. Clayson, 1992: Satellite-image-derived Gulf Stream currents compared with numerical model results. *J. Atmos. Oceanic Technol.*, **9**, 286–304.
- Godfrey, J. S., G. R. Cresswell, T. J. Golding, and A. F. Pearce, 1980: The separation of the East Australian Current. *J. Phys. Oceanogr.*, **10**, 430–440.
- Holyer, R. J., and S. H. Peckinpaugh, 1989: Edge detection applied to satellite imagery of the oceans. *IEEE Trans. Geosci. Remote Sens.*, **27**, 46–56.
- Kelly, K. A., 1989: An inverse model for near-surface velocities from infrared images. *J. Phys. Oceanogr.*, **19**, 1845–1864.
- , and P. T. Strub, 1992: Comparison of velocity estimates from Advanced Very High Resolution Radiometer in the coastal transition zone. *J. Geophys. Res.*, **97**, 9653–9668.
- Kriebel, K. T., R. W. Saunders, and G. Gesell, 1991: Optical properties of clouds derived from fully cloudy AVHRR pixels. *Contrib. Atmos. Phys.*, **42**, 1–471.
- LeTraon, P. Y., and F. Hernandez, 1992: Mapping the oceanic mesoscale circulation: Validation of satellite altimetry using surface drifters. *J. Atmos. Oceanic Technol.*, **9**, 687–698.
- Liu, A. K., S. Marine, and R. Kwok, 1997: Tracking of ice edges and ice flows by wavelet analysis of SAR images. *J. Atmos. Oceanic Technol.*, **14**, 1187–1198.
- Mata, M. M., M. Tomczak, S. Wijffels, and J. A. Church, 2000: East Australian Current volume transport at 30°S: Estimates from the World Ocean Circulation Experiment hydrographic sections PR11/P6 and the PCM3 current meter array. *J. Geophys. Res.*, **105**, 28 509–28 526.
- Nilsson, C. S., and G. R. Cresswell, 1981: The formation and evolution of East Australian Current warm-core eddies. *Progress in Oceanography*, Vol. 9, Pergamon Press, 133–183.
- Ohlmann, J. C., P. P. Niiler, C. A. Fox, and R. R. Leben, 2001: Eddy energy and shelf interactions in the Gulf of Mexico. *J. Geophys. Res.*, **106**, 2605–2620.
- Ridgway, K. R., J. R. Dunn, and J. L. Wilkin, 2002: Ocean interpolation by four-dimensional weighted least squares—Application to the waters around Australasia. *J. Atmos. Oceanic Technol.*, **19**, 1357–1375.
- Schmetz, J., and M. Nuret, 1987: Automatic tracking of high-level clouds in Meteosat infrared images with a radiance windowing technique. *Eur. Space Agency J.*, **11**, 275–286.
- Strub, P. T., T. K. Chereskin, P. P. Niiler, C. James, and M. D. Levine, 1997: Altimeter-derived variability of surface velocities in the California Current system. *J. Geophys. Res.*, **102**, 12 727–12 748.
- Tokmakian, R., P. T. Strub, and J. McClean-Padman, 1990: Evaluation of the maximum cross-correlation method of estimating sea surface velocities from sequential satellite images. *J. Atmos. Oceanic Technol.*, **7**, 852–865.
- Vigan, X., C. Provost, R. Bleck, and P. Courtier, 2000a: Sea surface velocities from sea surface temperature image sequences 1. Method and validation using primitive equation model output. *J. Geophys. Res.*, **105**, 19 499–19 514.
- , —, and P. Podesta, 2000b: Sea surface velocities from sea surface temperature image sequences 2. Application to the Brazil–Malvinas Confluence area. *J. Geophys. Res.*, **105**, 19 515–19 534.
- Wilkin, J. L., M. M. Bowen, and W. J. Emery, 2002: Mapping mesoscale currents by optimal interpolation of satellite radiometer and altimeter data. *Ocean Dynamics*, **52**, 95–103.
- Zavialov, P. O., R. D. Ghisolfi, and C. A. E. Garcia, 1998: An inverse model for seasonal circulation over the southern Brazilian shelf: Near-surface velocity from the heat budget. *J. Phys. Oceanogr.*, **28**, 545–562.



